PCCP

PAPER

View Article Online
View Journal | View Issue

Cite this: *Phys. Chem. Chem. Phys.*, 2018, **20**, 20257

Multifunctional nanostructured Co-doped ZnO: Co spatial distribution and correlated magnetic properties

Rafael T. da Silva,[a] Alexandre Mesquita,[b] Angela O. de Zevallos,[ac] Thalita Chiaramonte,[d] Xavier Gratens,[e] Valmir A. Chitta,[e] Juliana M. Morbec,[af] Gul Rahman,[g] Victor M. García-Suárez,[hi] Antonio C. Doriguetto,[c] Maria I. B. Bernardi[j] and Hugo B. de Carvalho *[a]

Received 5th May 2018,
Accepted 8th July 2018

DOI: 10.1039/c8cp02870b

rsc.li/pccp

In this report we present a systematic structural and magnetic analysis of Co-doped ZnO nanoparticles prepared *via* a microwave-assisted hydrothermal route. The structural data confirm the incorporation of Co ions into the wurtzite ZnO lattice and a Co concentration mainly near/at the surface of the nanoparticles. This Co spatial distribution is set to passivate the surface of the ZnO nanoparticles, inhibiting the nanoparticle growth and suppressing the observation of a ferromagnetic phase. Based on experimental and theoretical results we propose a kinetic-thermodynamic model for the processes of nucleation and growth of the Co-doped ZnO nanoparticles, and attribute the observed ferromagnetic order to a ferromagnetism associated with specific defects and adsorbed elements at the surface of the nanoparticle. Our findings give valuable contribution to the understanding of both the doping process at the nanoscale and the nature of the magnetic properties of the Co-doped ZnO system.

1. Introduction

The challenge of developing a new material technology to solve increasingly serious problems on the global scale, pertaining to the environment, energy, and resources, is being pursued actively. It is against such a backdrop that ZnO, which is a nontoxic abundant resource with superior environmental affinity, is drawing much attention. Nanostructured ZnO has been extensively investigated for its versatile physical and electrochemical properties, giving it a multifunctional performance across multiple applications. With a wide bandgap (3.4 eV) and a strong binding energy (~60 meV) at room temperature,[1] ZnO has been considered as an excellent material for UV lasers,[2] transparent conductive oxides (TCOs),[3] for application in catalysis,[4] and also for dye-sensitized solar cells.[5] The existence of various 1D and 2D forms of ZnO has also provided more opportunities for its use in energy harvesting,[6] including photovoltaic[7] and sensor applications.[8]

Specifically, magnetic nanostructured ZnO has also been considered for biomedical applications due to its low-toxicity as bioimaging, drug delivery[9] and antibacterial agents.[10] The desired magnetic properties can be achieved by doping the ZnO matrix with magnetic elements or by incorporating magnetic complexes. As prepared, the magnetic nanostructured ZnO would be functionalized as both fluorescent and magnetic probes. Here, the main problem concerns the fact that usually the doping of nanostructured ZnO with magnetic elements, such as Fe, Co, Ni, and Mn, for reasons shown later in this article, quenches the ZnO visible fluorescence that mainly arises from its surface defects.[11–13] Besides, magnetic ZnO is also emerging as a promising dilute magnetic semiconductor (DMS) to be used as a spin injection layer in spintronic semiconductor systems. Spintronics is currently attracting considerable attention because of its enormous potential in next-generation data storage and logic devices.[14] According to Dietl *et al.*,[15] Mn-doped ZnO and GaN, wide band gap semiconductors, theoretically would present Curie temperatures (T_C) above room temperature. However, the obtained results, especially for the TM-doped semiconductor oxides, regarding the

[a] *Instituto de Ciências Exatas, Universidade Federal de Alfenas – UNIFAL-MG, 37133-840 Alfenas, MG, Brazil. E-mail: bonette@gmail.com*
[b] *Departamento de Física, Instituto de Geociências e Ciências Exatas, Universidade Estadual Paulista – UNESP, 13500-900 Rio Claro, SP, Brazil*
[c] *Instituto de Química, Universidade Federal de Alfenas – UNIFAL-MG, 37133-840 Alfenas, MG, Brazil*
[d] *Departamento de Ciências Naturais, Universidade Federal de São João Del-Rei – UFSJ, 36301-160 São João Del-Rei, MG, Brazil*
[e] *Instituto de Física da Universidade de São Paulo, 05508-090 São Paulo, SP, Brazil*
[f] *Faculty of Physics, University of Duisburg-Essen, Duisburg 47057, Germany*
[g] *Department of Physics, Quaid-i-Azam University, Islamabad 45320, Pakistan*
[h] *Departamento de Física, Universidad de Oviedo, 33007 Oviedo, Spain*
[i] *Nanomaterials and Nanotechnology Research Center – CINN, Spain*
[j] *Instituto de Física de São Carlos, Universidade de São Paulo – USP, 13560-970 São Carlos, SP, Brazil*

nature of the often observed room temperature ferromagnetism (RTFM), are very controversial and inconclusive. Today there is a consensus that TM-doping is not a sufficient condition to achieve the RTFM[16,17] and that point defects play an important role in reaching a ferromagnetic order.[18–23] At the nanoscale, confinement of the dopants enhances their interactions with carriers and/or spins,[24] leading also to interesting properties like spin filtering.[25]

Concerning the doping process at the nanoscale, as pointed above, the use of intentional impurities, or dopants, to control the properties of materials is essential for many technologies. However, it is a well-known fact that the incorporation of dopants at the nanoscale is a very difficult task;[26] even for highly soluble dopants, the incorporation of a significant amount of dopant atoms during synthesis is not straightforward. Even when dopants are incorporated, their concentration is typically an order of magnitude less than that in the growth solution.[27] These results have led to theoretical efforts to understand the mechanisms that control the doping process.

In this context, the aim of the present report is to give further contribution to the understanding of the dopant incorporation process at the nanoscale and how it can affect some important properties of the materials, such as their magnetic behavior. Here nanostructured Co-doped ZnO ($Zn_{1-x}Co_xO$) samples were synthesized using a microwave-assisted hydrothermal method with Co concentration up to 7 at%. Among the TM elements used to dope ZnO, Co ions in principle can be easily incorporated into the wurtzite ZnO (w-ZnO) lattice, once they can assume the +2 oxidation state and a crystal radius quite close to that of Zn^{2+}. Considering the magnetic properties, Co has one of the highest magnetic moments (4.8 μ_B) and a positive magnetic exchange coupling constant in the metallic phase. This synthesis method combines the advantages of both hydrothermal and microwave-irradiation techniques, such as very short reaction times and the production of small particles with a narrow size distribution.[28] We performed a detailed structural analysis by conjugating several different techniques to fully characterize the structures of the samples. The relationships between the magnetic properties and the structure results of the nanostructured Co-doped ZnO ($Zn_{1-x}Co_xO$) samples are presented. First-principles calculations were also performed to gain insight into the mechanisms of Co incorporation into the ZnO nanocrystals and the observed magnetic properties.

2. Experimental methods

Nanostructured Co-doped ZnO ($Zn_{1-x}Co_xO$) samples were synthesized *via* a microwave-assisted hydrothermal route with Co nominal concentrations (x_N) of 0 (undoped), 0.5, 1, 3, 5 and 7 at% (x_N = 0, 0.005, 0.01, 0.03, 0.05 and 0.07). In a typical procedure to obtain the $Zn_{1-x}Co_xO$ nanostructures, 0.02 mol of $ZnCl_2$ and $CoCl_2$, maintaining the desired stoichiometric proportion between the cations, were dissolved in 50 mL of distilled water. Then, 50 mL of 10 mol L^{-1} NaOH solution was added rapidly under vigorous stirring. The mixed solution was placed in a 110 mL Teflon autoclave reaching 90% of its volume, which was sealed and placed in a microwave hydrothermal system, applying 2.45 GHz of radiation at a maximum power of 800 W, at a heating rate of 30 °C min^{-1}. The as-prepared solution was subjected to a microwave hydrothermal synthesis temperature of 160 °C for 10 min, and cooled in air at room temperature. After the hydrothermal reaction, the obtained precipitate powder was washed several times with distilled water and isopropyl alcohol and then dried at 60 °C for 24 h.

The crystal structures of the samples were characterized using X-ray diffraction (XRD) performed in the range of 2θ = 30°–80° in steps of 0.02° at 5 s per step using CuKα radiation (λ = 1.5418 Å) and a LiF(100) monochromator on a Rigaku Ultima IV diffractometer. The determination of the lattice parameters and the occupation factor over the structure was performed by using the Rietveld method as implemented by the General Structure Analysis System (GSAS) software package with the graphical user interface EXPGUI.[29,30] The morphology and the grain size distribution were determined using a JEOL JM-2100F high resolution transmission electron microscope (HRTEM); the effective Co concentration (x_E) was estimated by energy dispersive X-ray spectrometry (EDS), using an Oxford XMAX 50 detector; the spatial map of the Co distribution in the nanoparticles was obtained *via* electron energy-loss spectroscopy (EELS), using a GATAN GiF Tridiem 863 image filter; the structure of the samples was also evaluated by selected area electron diffraction (SAED). These analyses were conducted at the Brazilian Nanotechnology National Laboratory (LNNano). Raman scattering spectroscopy was used to study the incorporation of dopants and the resulting lattice disorder in the w-ZnO host structure. Raman measurements were carried out at room temperature on a Jobin-Yvon-64000 micro-Raman system in the backscattering geometry, using the 488 nm line of an Ar^+ laser for excitation. X-ray absorption spectroscopy (XAS) analysis was employed to determine the oxidation state (XANES – X-ray Near-Edge Spectroscopy) and to assess the environment (EXAFS – Extended X-ray Absorption Fine Structure) of the Co atoms in the w-ZnO structure. These measurements were performed at the Co K-edge in transmission mode using a Si(111) channel-cut monochromator at the XAFS2 beamline of the Brazilian Synchrotron Light Laboratory (LNLS). We have employed the Multiplatform Applications for XAFS (MAX)[31] software package and the FEFF9 code[32] in the EXAFS analyses. Magnetic measurements were performed using a superconducting quantum interference device magnetometer (SQUID).

3. Theoretical calculations

The structural and magnetic properties of the nanostructured $Zn_{1-x}Co_xO$ samples were also investigated by means of first-principles calculations based on density functional theory (DFT).[33] Spin-polarized calculations were performed using the local density approximation (LDA),[34,35] which has been used in previous first-principles calculations of ZnO nanoparticles.[36,37]

We used the Siesta code,[38] which employs norm-conserving Troullier–Martins pseudopotentials[39] and linear combinations of atomic orbitals. We used a double-zeta basis set with polarization functions (DZP) for all atoms and a real-space energy cutoff of 200 Ry. We considered w-ZnO nanoparticles with 80 atoms (40 Zn and 40 O), simulated within the supercell approach with a vacuum of ~10 Å between the nanoparticle and its image. The dangling bonds at the surface of the nanoparticle were kept unsaturated and the atoms were allowed to relax to their minimum energy configurations. One and two substitutional Co impurities at Zn sites were considered, which correspond to Co concentrations of 2.5 and 5.0%, respectively; these concentrations are in the range of the samples studied in this report (between 0.5 and 7%). All atomic positions were fully relaxed until the forces on each atom were smaller than 0.02 eV $Å^{-1}$.

4. Results and discussion

4.1. X-ray diffraction

Fig. 1 shows the experimental X-ray diffraction (XRD) and the theoretical refined Rietveld patterns obtained for the studied set of samples. The difference between the experimental and fitted patterns is also presented in Fig. 1. All the observed diffraction peaks are indexed to those of the hexagonal w-ZnO structure, with space group $P6_3mc$ (JCPDS 36-1451). No traces of metallic Co or any other secondary phases can be detected within the XRD detection limit. The Rietveld refinement was performed by taking initially the Zn^{2+} and O^{2-} ions located at (1/3, 2/3, 0) and (1/3, 2/3, z), respectively. Table 1 presents the fitted cell parameters and the Rietveld statistics (χ^2 and R_B), which indicate good agreement between the experimental and calculated patterns. We do not observe any changes in the cell parameters as a function of doping and these data are very similar to those reported for pure ZnO.[40] The Rietveld results are an indication that the crystal radius of the Co ions in the samples is quite close to that of the Zn^{2+} ions in the w-ZnO lattice (0.74 Å).[41] In fact, by considering that the Co ion in the samples has a +2 oxidation state and takes the tetrahedral sites of the Zn^{2+} in the w-ZnO lattice (substitutional doping), its crystal radius is 0.72 Å,[41] a value that would lead to only small or insignificant changes in the w-ZnO structure, as observed. Therefore, the XRD results indicate that the Co ions in our nanostructured $Zn_{1-x}Co_xO$ samples have a +2 oxidation state and are located at the sites of the Zn^{2+} cations (Wyckoff position) with no secondary or segregated phases. The +2 oxidation state of the Co ions was further confirmed from the local structure analysis performed *via* X-ray absorption measurements (XANES). Our DFT calculations also found no significant changes in the w-ZnO structure assuming the Zn substitutional character of Co doping.

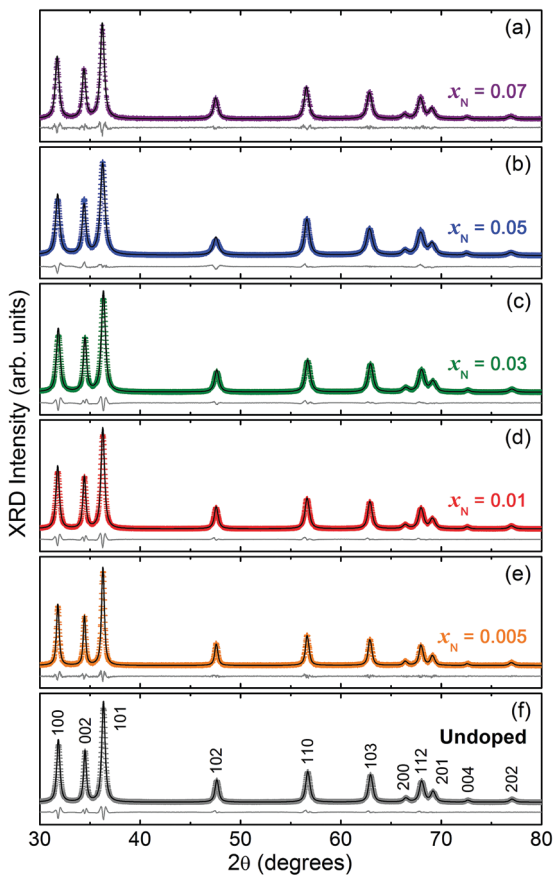

Fig. 1 Refined XRD diffractograms of the nanostructured $Zn_{1-x}Co_xO$ samples: (a) x_N = 0.07, (b) 0.05, (c) 0.03, (d) 0.01, (e) 0.005 and (f) undoped ZnO. Each figure shows the observed pattern (symbols), Rietveld calculated pattern (solid line), and the goodness of the fit or residual pattern (at the bottom).

Table 1 Structural data (*a* and *c*) for the nanostructured $Zn_{1-x}Co_xO$ samples obtained through the Rietveld refinement. *V* is the cell volume, χ^2 is the square of the goodness-of-fit indicator, and R_B is the refinement quality parameter. x_N is the nominal Co concentration

x_N	*a* (Å)	*c* (Å)	*V* (Å^3)	χ^2	R_B
Undoped	3.2532(4)	5.213(1)	47.776(1)	8.33	1.47
0.005	3.2545(4)	5.215(1)	47.835(1)	8.48	1.90
0.010	3.2538(4)	5.213(1)	47.798(1)	8.72	1.49
0.030	3.2540(4)	5.213(1)	47.803(1)	8.43	1.46
0.050	3.2553(1)	5.218(1)	47.889(1)	8.11	2.19
0.070	3.2560(1)	5.215(1)	47.878(1)	9.77	2.42

Table 2 presents the elemental occupation factors obtained also from the Rietveld refinement. Estimated concentrations of defects related to vacant sites and the Co concentration in the samples can be inferred from the occupation factors. It is observed that the Co content is quite close to the Co nominal

Table 2 Elemental occupation factor for the nanostructured $Zn_{1-x}Co_xO$ samples obtained through Rietveld refinement

x_N	Zn	Co	Zn + Co	O
Undoped	1.001(1)	—	—	0.997(5)
0.005	0.996(2)	0.004(2)	1.000(4)	0.990(1)
0.010	0.991(1)	0.012(1)	1.003(2)	0.988(5)
0.030	0.972(1)	0.039(1)	1.011(2)	0.982(5)
0.050	0.957(1)	0.056(1)	1.013(2)	0.979(4)
0.070	0.929(3)	0.071(3)	1.000(6)	0.990(1)

concentration (x_N) and there is no detection of significant vacancies at both Zn and O sites. However, considering the intrinsic errors involved in the refinement process, we can state, at least, a low density of such kind of defect in our set of samples.

4.2. Electron microscopy and elemental analyses

The morphology of the samples was evaluated by means of transmission electron microscopy (TEM) measurements. Fig. 2(a) shows a representative TEM micrograph for the sample with $x_N = 0.07$. In general, the set of samples are composed of round shaped (multifaceted) nanoparticles with a diameter of less than 30 nm. SAED measurements were also performed (inset in Fig. 2(a)). Fig. 2(b) present the corresponding azimuthal integration along the interplanar distance. Here, all the observed diffraction peaks are associated with the w-ZnO structure. To check the effective Co concentration in the nanostructured $Zn_{1-x}Co_xO$ samples, as well as to probe the possible presence of secondary phases, fractions of the samples were cold pressed in the form of pellets and EDS analyses were carried out over large areas on the surface of the pellets. The measured average effective Co concentrations (x_E) listed in Table 3 are in good agreement with the nominal stoichiometry (x_N) of the samples. It is worth pointing out that EDS analyses, within their detected limits, do not reveal evidence of any crystallographic secondary phase. These results also suggest that the Co ions in the studied samples substitute Zn^{2+} ions into the w-ZnO lattice, in good agreement with XRD results.

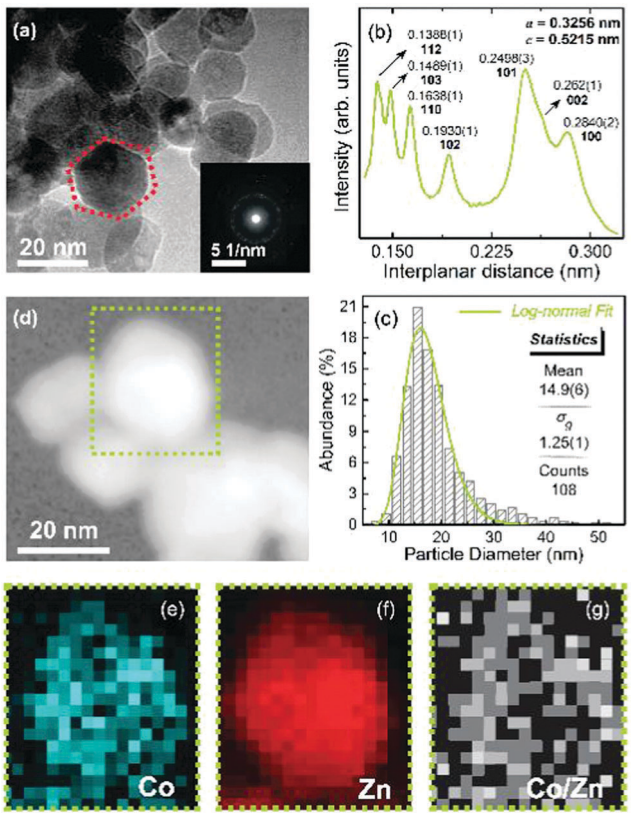

Fig. 2 (a) Representative TEM micrograph of nanostructured $Zn_{1-x}Co_xO$ sample with $x_N = 0.07$. The inset in (a) shows a SAED pattern obtained for this sample, and (b) the corresponding azimuthal integration intensity as a function of the interplanar distance. The cell parameters *a* and *c* were taken from the Rietveld refinement results (Table 1). (c) Particle size distribution histogram. The line in panel (c) is the log-normal fit. (e) Cobalt and (f) zinc elemental mapping obtained by EELS in the grain highlighted in the TEM micrograph in panel (d) by the dotted green line. (g) Co/Zn intensity ratio map (dark pixels correspond to smaller Co/Zn ratios).

Table 3 Particle size distribution analyses. *d* is the mean value of the particle diameter and σ_g is the geometric standard deviation obtained by the log-normal fit of particle size distribution histograms for each sample. *N* is the total number of counted particles. x_E is the effective Co concentration measured by EDS. The presented error for the x_E data corresponds to the standard error of the mean

x_N	x_E	*d* (nm)	σ_g	*N*
Undoped	—	26.5(4)	1.40(7)	253
0.005	0.006(2)	26.4(5)	1.32(3)	300
0.010	0.011(2)	19.3(4)	1.35(3)	280
0.030	0.027(3)	18.3(4)	1.35(3)	208
0.050	0.055(2)	16.9(1)	1.42(6)	589
0.070	0.072(4)	14.9(6)	1.25(1)	108

Fig. 2(c) shows the obtained histogram used for the statistical analyses of the grain diameter distribution. The images and statistical data for the other samples are similar to those shown in Fig. 2(a)–(c) and are summarized in Table 3. We observe that by increasing the Co content the mean diameter of the nanoparticles decreases. Such behavior has already been reported in nanostructured systems based on ZnO,[42] SnTe[43] and also on TiO_2 in the anatase phase doped with Eu[44] and La.[45] The Co spatial distribution in the nanoparticles was also mapped *via* state-of-the-art elemental analysis by means of electron energy-loss spectroscopy (EELS). We followed the procedures described by Wang *et al.*[46] The obtained results are presented in Fig. 2(e)–(g). The bright edges in Fig. 2(g), which correspond to the Co/Zn ratio, reveal the Co richness near/at the surface (outer shells) of the nanoparticle. The same analysis on other nanoparticles confirms the inhomogeneity of the Co distribution. The magnetic results (discussed in Section 4.5) also indicate an inhomogeneity in Co distribution along the volume of the nanoparticles.

Generally, the growth of nanoparticles depends on the diffusion of the monomers in the precursor solution to the surface of the growing nanoparticle and on the surface reaction.[47] Thus, the concentration of the Co ions on the surface of the nanoparticles explains the decrease of the mean diameter with the increase in the Co content by an effect of surface passivation. This kind of effect has been reported previously by different capping/passivating agents.[48–50] The passivation of the ZnO surface by the Co ions also explains the usually observed reduction of the ZnO photocatalytic activity upon doping with Co and other transition metals (TM) in relatively small (<50 nm) nanoparticles[51–53] and, as mentioned in the Introduction section, also explains the quenching of the ZnO visible fluorescence by the passivation of the corresponding surface defects.[11–13]

4.3. Raman scattering spectroscopy

Raman spectra from our nanostructured $Zn_{1-x}Co_xO$ samples are shown in Fig. 3(a) and (b). The spectra were normalized by

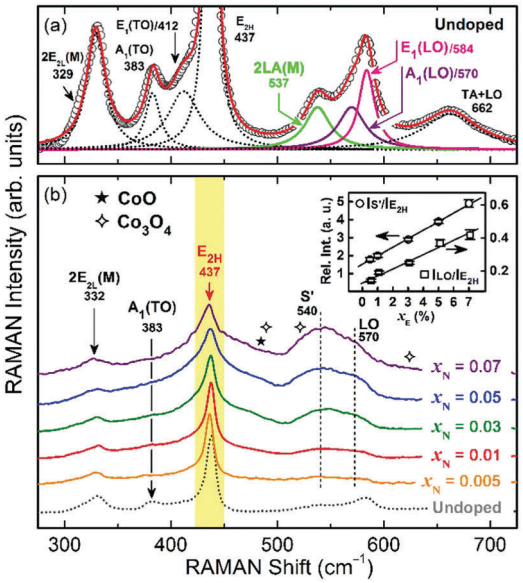

Fig. 3 Raman scattering spectra obtained at room temperature for the nanostructured (a) undoped ZnO and (b) $Zn_{1-x}Co_xO$ samples. The spectra were acquired at room temperature and are normalized by the E_{2H} vibrational mode. The spectrum for the undoped sample is also shown in (b) for comparison. The inset (b) presents the relative intensity of the S′ and LO modes as a function of the effective Co concentration (x_E). The intensities were obtained *via* multipeak Lorentz fittings. The symbols ★ and ✧ mark the position of the main modes related to the Co oxides, CoO end Co_3O_4, respectively.[16]

the main vibrational mode E_{2H}. For the undoped ZnO sample (Fig. 3(a)) we observe a series of modes centered at 329, 383, 412, 437, 537, 570, 584 and 662 cm^{-1}, that are assigned to the first and second order w-ZnO modes: $2E_{2L}$ at the *M*-point of the Brillouin zone (BZ), A1(TO), E1(TO), E_{2H}, 2LA also at the *M*-point of the BZ, A_1(LO), E_1(LO) and TA + LO, respectively.[54] A significant result from the Raman data for the doped samples (Fig. 3(b)) is the complete absence of modes related to segregated secondary phases (CoO and Co_3O_4). The Raman scattering results, together with the XRD data and the electron microscopy analysis, are strong evidence that Co ions in our samples are incorporated into the w-ZnO lattice. Special attention has to be paid to the broad band between 500 and 600 cm^{-1}. This broad band encloses several modes, whereas the main ones are centered approximately at 540 (S′, left shoulder) and 570 cm^{-1} (LO, right shoulder).

We observe that the relative intensity of these modes scales linearly with Co content in the samples (inset of Fig. 3(b)), in agreement with our previous results reported for Co-doped ZnO bulk ceramics.[16] The appearance of this broad band and its dependence on the dopant concentration are also observed for different doping elements: H,[55] N,[55,56] P,[57] Mn,[58] Ni,[59] Cu,[60] Ga,[56] Ag,[61] and Sb,[62] just to mention a few. There are also reports showing the activation of these modes in undoped ZnO *via* mechanical milling.[63,64] Special remarks can be made considering ion implanted ZnO samples where, besides the dopant incorporation, the irradiation process leads to inevitable structural defects, and that after annealing the broad band completely disappears.[56,57] These data lead us to infer that the observation of these modes is related to structural defects introduced in the w-ZnO lattice due to the dopant incorporation or due to the extrinsic structural damage. However, it is interesting to note that the nature of the modes in the observed broad band is different. Doped ZnO samples usually exhibit a more pronounced left shoulder,[16] as in the present case; besides, for structurally damaged samples, on the other hand, the right shoulder is more intense.[56,63] And, in fact, the indexation of the vibrational modes in this region of the spectrum is a highly controversial issue. Schumm *et al.*[58] identified for the $Zn_{1-x}Mn_xO$ system at the left shoulder the presence of an activated ZnO mode at 528 cm^{-1}, tentatively assigned to the $2B_{1L}$ mode, and an additional mode at 519 cm^{-1} that could be assigned to the local vibrational mode (LVM) of Mn substitutionally incorporated into the w-ZnO lattice. In turn, the mode at 570 cm^{-1} can be attributed to the overlap of the LO phonons of the A_1 (predominant) and E_1 modes. In pure ZnO, the A_1(LO) and E_1(LO) modes are usually very weak (Fig. 3(a)) due to the destructive interference between the deformation and the Frölich potentials.[65] Nevertheless, the scattering cross section of these modes can be amplified by the presence of intermediate electronic states in the band gap related to bound excitons created due to the introduction of defects and impurities,[55] an extrinsic Frölich interaction.[66]

4.4. X-ray absorption

Fig. 4 shows the XANES spectra obtained for the nanostructured $Zn_{1-x}Co_xO$ samples at the Co K-edge and for reference Co oxides (vertically shifted for clarity). We observe in the spectra that the Co absorption edge for the studied samples compares with that of the CoO reference sample, which leads us to conclude that the Co ions predominantly have a +2 oxidation state in our nanostructured samples. All the spectra have similar features, an indication that there is no significant structural distortion around the Co ions for different doping levels; similar behavior was also observed in the DFT calculations when all the atoms

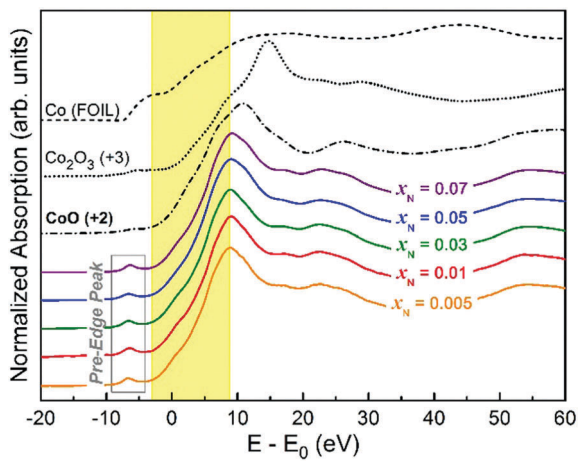

Fig. 4 Co K-edge XANES spectra of the nanostructured $Zn_{1-x}Co_xO$ samples (E_0 = 7708.8 eV). Spectra of metallic Co, rocksalt CoO (oxidation state +2) and Co_2O_3 (oxidation state +3) are also shown for comparison.

Table 4 Co K-edge EXAFS simulation results obtained by assuming the Co^{2+} ions at Zn^{2+} sites in the ZnO matrix. *R* is the distance from the central atom, *N* is the average coordination number, σ^2 the Debye–Waller factor and QF the quality factor

x_N	Shell	*R* (Å)	*N*	σ^2 ($\times 10^{-3}$ Å^2)	QF
0.005	Co–O	1.99(2)	4.7(7)	8(2)	3.52
	Co–Zn	3.19(4)	6(4)	9(1)	
	Co–Zn	3.23(7)	5(3)	9(1)	
	Co–O	3.75(2)	10(2)	8(2)	
0.01	Co–O	1.95(1)	4.2(7)	6(2)	1.67
	Co–Zn	3.20(5)	5(7)	8(1)	
	Co–Zn	3.22(7)	5(4)	8(1)	
	Co–O	3.72(2)	8(4)	6(2)	
0.03	Co–O	1.97(1)	4.2(6)	5(2)	1.27
	Co–Zn	3.22(1)	5(2)	7(3)	
	Co–Zn	3.20(3)	4(4)	7(3)	
	Co–O	3.72(3)	11(2)	5(2)	
0.05	Co–O	1.98(2)	4.4(6)	7(2)	0.98
	Co–Zn	3.21(1)	6(3)	8(3)	
	Co–Zn	3.10(6)	1(1)	8(3)	
	Co–O	3.71(2)	10(2)	7(2)	
0.07	Co–O	1.99(1)	4.3(6)	6(2)	1.14
	Co–Zn	3.22(1)	9(1)	9(1)	
	Co–Zn	3.28(3)	2(1)	9(1)	
	Co–O	3.77(2)	8(2)	6(2)	

around Co are relaxed. The calculated bond length of Co–O is 1.93 Å (comparable with the extracted EXFS data presented in Table 4) which is only slightly smaller than the calculated Zn–O bond length of ~2.0 Å. Similarly, no significant change in the bond angles was observed *via* DFT calculations: the O–Co–O bond angle is 124°, which is comparable with the O–Zn–O bond angle of 125°.

We also note a small absorption peak at the pre-edge region. The Co K-edge absorption spectrum is related to electronic transitions from the 1s ($l = 0$) state to the 4p ($l = 1$) empty states. Besides, the pre-edge region is related to electronic transitions from the 1s to 3d ($l = 2$) states. Although this transition is originally forbidden ($\Delta l \neq \pm 1$), it occurs due to the hybridization of the Co 3d states with O 2p in the sites without an inversion center of symmetry.[67] In the wurtzite structure the Zn ions assume a +2 oxidation state and are located in tetrahedral sites, with no inversion center of symmetry, surrounded by four O^{2-} ions. Therefore, the +2 oxidation state for the Co ions and the observation of the pre-edge peak strongly indicate that the Co ions occupy the Zn ion sites in the lattice of our nanostructured w-ZnO samples.

Fig. 5 presents the modulus of the k^3 weighted Fourier transforms (FT) that were extracted from the Co K-edge spectra for the nanostructured $Zn_{1-x}Co_xO$ samples, Co foil and Co oxides and the spectrum obtained at the Zn K-edge for an undoped ZnO sample. The obtained data reveal that qualitatively there are no significant changes in the crystallographic environment for the Co-doped samples as a function of the Co-doping. In addition, these data are also quite different from those obtained for the Co references (Co foil and Co oxides), and, in contrast, resemble the obtained data for the undoped

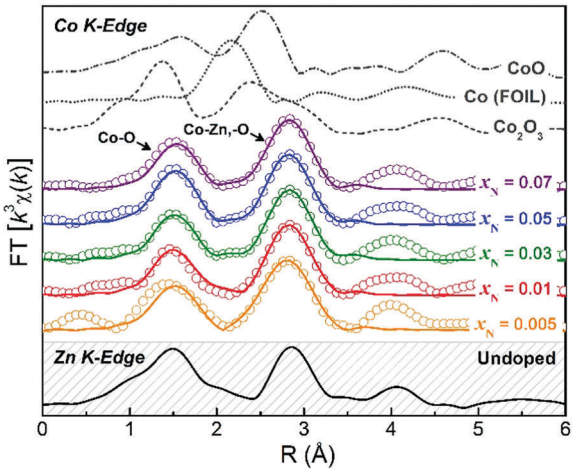

Fig. 5 Corresponding k^3 weighted Fourier transforms (FT) of the X-ray absorption spectra obtained at Co and Zn K-edge for the nanostructured $Zn_{1-x}Co_xO$ samples and reference materials. Open symbols are the experimental data and the solid lines represent the fittings using the parameters shown in Table 2. The spectra are offset for clarity.

ZnO sample at the Zn K-edge. These observations led us to conclude that the Co^{2+} ions in the doped samples are placed in the Zn^{2+} sites in the w-ZnO lattice. Theoretical analyses of the Fourier transforms for the Co-doped samples were performed *via* Multi-Platform Applications for X-ray absorption (MAX)[31] and the FEFF9 code.[32] Details of the procedures were described before.[68] In Fig. 5 good agreement between experimental data (symbols) and theoretical results (lines) is observed. Table 4 lists the parameters obtained from the best fits to the data. The first shell (Co–O) coordination number is 4, consistent with a substitution for tetrahedral Zn^{2+} ions in the w-ZnO structure; additionally, according to our calculations the interatomic distances are not affected by the Co-doping, confirming the XRD Rietveld, XANES structural analyses, and also consistent with our DFT calculations.

In summary, the structural analysis confirms that the Co^{2+} ions occupy the Zn-sites of the w-ZnO lattice in our nanostructured $Zn_{1-x}Co_xO$ samples. Clearly the results exclude the presence of magnetic extrinsic sources, such as Co-rich nanocrystals or segregated secondary magnetic phases. The size distribution analysis and the EELS results point out that, in spite of the Zn substitutional character of the Co-doping, the Co distribution is not homogeneous, concentrating near/at the surface of the nanoparticles. With these conclusions we proceed to the magnetic characterization.

4.5. Magnetic characterization

The magnetic behavior of the studied samples shows features of a paramagnetic phase with a large antiferromagnetic (AF) exchange interaction between Co^{2+} ions. This behavior is similar to other studied diluted magnetic semiconductors (DMS).[69–73] However, for the undoped ZnO sample and for the samples with lower Co concentration ($x \leq 0.01$), a small ferromagnetic (FM) contribution was detected at $T = 300$ K. Fig. 6 presents the $M(H)$ for the undoped ZnO, $x_N = 0.005$ and

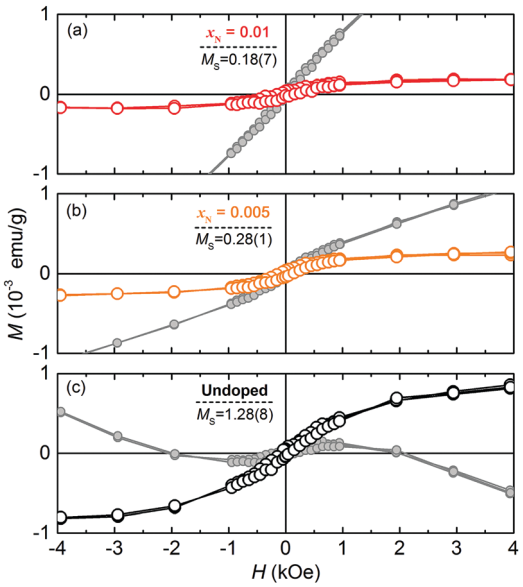

Fig. 6 Low field part of the magnetization traces obtained at T = 300 K for the (a) x_N = 0.01, (b) x_N = 0.005 and (c) undoped ZnO samples. The gray small full symbols correspond to the raw data obtained for the samples before the subtraction of the main diamagnetic (undoped, (a)) and main paramagnetic (doped, (b) and (c)) contributions.

x_N = 0.01, samples and the corresponding obtained M_S values. The parameter M_S is the saturation magnetization of the FM contribution. The extraction of the magnetic susceptibility (χ) for the cobalt paramagnetic phase and saturation magnetization (M_S) of the FM phase have been realized using the following method. The magnetization (M) has been measured at a fixed temperature for various low field values above the saturation field of the FM contribution. The collected ramp of M was fitted by a linear regression ($M = M_S + \chi_{PD}H$). The angular coefficient χ_{PD} is the susceptibility of the paramagnetic phase (χ_P) plus the diamagnetic contribution (χ_D) of the ZnO lattice ($\chi_{PD} = \chi_P + \chi_D$). For all samples, the fit yielded a constant diamagnetic susceptibility (χ_D) similar to the ZnO sample, $\chi_D = -3.45 \times 10^{-7}$ (emu g^{-1}). By this way it was verified that M_S is independent of T. For the other samples, no FM contribution has been detected ($M_S \approx 0$).

One can find in the literature a great number of reports on ferromagnetism in undoped ZnO systems.[74,75] The often observed small FM phase is usually discussed in terms of d^0 ferromagnetism.[76] Here, point defects (vacancies or interstices) are the responsible ones for the observed ferromagnetism by means of a spin polarized density of states around the Fermi level. It is a spin–split impurity band derived from defect states. In this context, many reports argue that the observed ferromagnetism is related to oxygen vacancies (V_O),[77–79] but there are also significant reports considering zinc vacancies (V_{Zn}),[80–82] revealing the controversial nature of this issue. Besides, Sundaresan *et al.* suggested that all metal oxides in the nanoparticulate form would exhibit room-temperature ferromagnetism due to the exchange interactions between unpaired electron spins arising from V_O at the nanoparticle surface.[74] Xu *et al.* showed that defects (V_O) located mainly near the surface would be the source of the observed RTFM in undoped ZnO nanoparticles.[79] From the theoretical point of view, Schoenhalz *et al.* proposed that the ferromagnetism in nanostructured materials would be mediated by extended defects, such as surfaces and grain boundaries.[37] In fact, one can find several reports arguing in favor of this kind of surface magnetism in several different systems.[83–86] In summary, the origins of magnetism in defective oxides are still under debate.

In order to understand the magnetic results for the undoped ZnO sample, we have performed DFT calculations on the formation energy (E_f) and the magnetic moments of V_{Zn} and V_O in the volume (v) and in the surface (s) of the ZnO nanoparticles. The defect formation energy is given by $E_f = E_{T,D} - E_T - \mu_X$, where $E_{T,D}$ is the total energy of the nanocrystal with the defect, E_T is the total energy of the nanocrystal without the defect, and μ_X is the chemical potential of X (X = Zn or O). The obtained values are presented in Table 5. We observe that defects (V_{Zn} and V_O) located in the surface of the nanoparticle have smaller formation energies than those in the volume region. Besides, only V_{Zn} presents magnetic moment both in the volume (1.95 μ_B per cell) and in the surface (2.00 μ_B per cell) of the nanoparticle. Systems with V_O have zero magnetic moment. These results lead us to conclude that only V_{Zn} would contribute to the observed ferromagnetic phase, and that the concentration of these defects would be higher at the surface of the nanoparticles.

For the Co-doped samples, we have also solved the Kohn–Sham (KS) equations in the FM and AF states and we have calculated the energy difference ($\Delta E = E_{FM} - E_{AF}$) as a function of Co–Co separation. At short distances lower than ~4 Å the dominant interactions between the Co atoms are AF, consistent with our experimental observations. The value of ΔE can be mapped into a mean field model and one can easily extract the exchange integral constant J, which is negative in all cases. For distances larger than ~4 Å a weak FM interaction appears. For two Co ions in a nanoparticle separated by more than 4 Å the calculated magnetic moment was 6.16 μ_B per cell. These data, together with the knowledge of the Co agglomeration in the region near/at the surface of the ZnO nanoparticles, allow us to state that a Co ferromagnetic order would be possible only at very low Co concentrations. We also examined the influence of V_{Zn} on the exchange interactions between the Co atoms, and we found that Co atoms prefer AF interactions even in the presence of V_{Zn}.

Table 5 DFT calculated formation energies (E_f) for the zinc (V_{Zn}) and oxygen (V_O) vacancies under Zn-rich and O-rich conditions in the volume (v) region and at the surface (s) of the ZnO nanoparticle. M is the corresponding calculated magnetic moment in units of Bohr magneton per cell

Defect		E_f (eV) Zn-Rich	E_f (eV) O-Rich	M (μ_B per cell)
V_{Zn}	v	3.62	0.46	1.95
	s	3.41	0.25	2.00
V_O	v	0.63	3.79	0.00
	s	0.42	3.59	0.00

Based on our DFT results we do not consider the contribution of the V_O for the observed RTFM and infer that it is, at least in part, related to the V_{Zn} at the surfaces of the nanoparticles. However, for the undoped ZnO sample we have measured a saturation magnetization of 1.28×10^{-3} emu g^{-1}, considering the calculated magnetic moment associated with V_{Zn} of 1.95 μ_B; the density of V_{Zn} (N_{Zn}) is estimated to be 10^{17} cm^{-3}. Besides, the N_{Zn} can also be estimated by the relation $N_{Zn} = N \times \exp(-E_f/k_BT)$, where N is the number of sites per cm^{-3}, E_f is the calculated formation energy for the V_{Zn}, k_B is the Boltzmann constant and T is the temperature. At 300 K, and taking into account the calculated E_f listed in Table 5, under the best conditions, the calculated N_{Zn} is not more than 10^{14} cm^{-3}. With these simple estimates we conclude that the observed RTFM for the undoped ZnO sample also cannot be fully explained in terms of the magnetic moments obtained in our DFT calculation. However, for the Co-doped samples (x_N = 0.005 and 0.01) the FM phase decreases drastically and disappears for higher Co concentration. Once the magnetic coupling between the Co ions is mainly of AF character, and taking into account the electron microscopy results, showing that the Co ions are concentrated near/at the surface of the nanoparticles, leading to a passivated surface, we arrive at the important conclusion that the observed RTFM in our samples is, in fact, mainly due to surface effects, a kind of surface magnetism related to different defects (not V_{Zn} and V_O), and possibly adsorbed elements.

The analysis of the paramagnetic phase measured for the set of Co-doped samples also gives us very important information. Fig. 7(a) shows the inverse of the paramagnetic susceptibility (χ_P^{-1}) as a function of the temperature. The diamagnetic contribution of the ZnO lattice has been subtracted from the data. For all samples, the magnetic susceptibility displays a Curie–Weiss (CW) behavior in the high-temperature range (120–300 K); $\chi_P = C/(T - \theta)$, where C is the Curie constant and θ is the CW temperature. Here we label the Co concentration derived from the paramagnetic component analyses as x_P in order to distinguish it from the nominal (x_N) and the measured effective (x_E) concentration. The Curie constant is related to the concentration through $C = N(g\mu_B)^2S(S + 1)x_P/3k_B$, where N is the number of cations per gram, g = 2.264 and S = 3/2 are respectively the isotropic Landé factor and the spin of the Co^{2+},[87,88] μ_B is the Bohr magneton and k_B is the Boltzmann constant.

From the fit of the χ_P to the CW law we obtain the Co concentration (x_P) in good agreement with x_N and x_E: x_P = 0.0055, 0.0102, 0.030, 0.052 and 0.071. These results are also an indication in favor of the previous conclusion that the observed RTFM for the undoped sample and for the samples with Co concentration of x_N = 0.005 and 0.01 is, in fact, not related to the Co doping, since almost all the Co ions in the samples are found in the paramagnetic state. Besides, the values of the CW temperature obtained for all the samples are displayed in Fig. 7(b) as a function of x_P. Negative values of θ indicate that the dominant exchange interaction between Co ions is antiferromagnetic, in accordance with the DFT results. Assuming here a linear dependence of θ with the concentration ($\theta = \theta_0 \times x_P$) we obtained $\theta_0 = -557 \pm 75$ K. The exchange constant of first neighbors (J_1) can be estimated using the relation $\theta_0 = 2zS(S + 1)J_1/3k_B$, where z is the coordination number (z = 12 for first neighbors in the wurtzite lattice). The obtained value of $J_1/k_B = -18.6 \pm 2.5$ K is in quite good agreement with previous reports.[16,89,92,93]

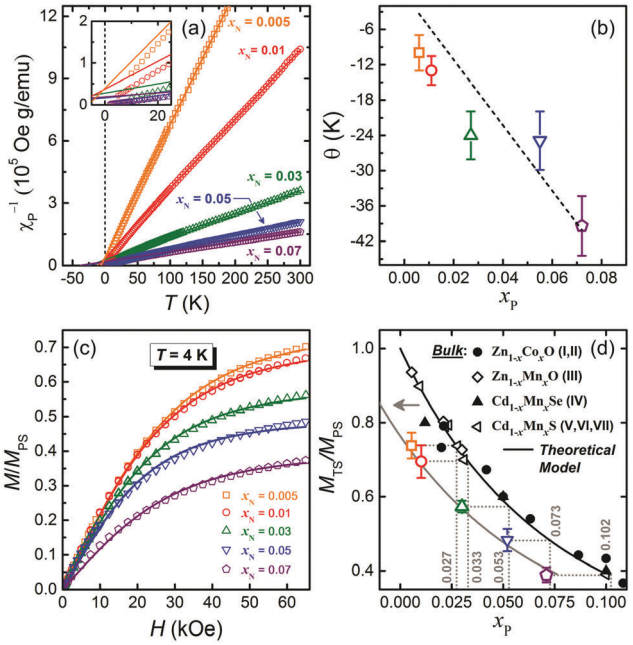

Fig. 7 (a) Inverse paramagnetic susceptibility (χ_P^{-1}) *vs.* temperature of the paramagnetic phase for the nanostructured $Zn_{1-x}Co_xO$ samples. Symbols are the experimental data. The solid lines represent the fit of the data in the high-temperature range to the CW law. The inset highlights the region of low temperature. (b) Experimental $\theta(x_P)$ obtained from the fit in (a) for all the studied samples. The dashed line represents the result of a linear fit of the experimental data. (c) Magnetization (M) of the samples measured as a function of the magnetic field (H) at T = 4 K. M is normalized to its saturation value M_{PS} calculated from results of the susceptibility. The symbols represent the experimental results and the lines display fits of the data by using a modified Brillouin function (MBF). (d) Ratio M_{TS}/M_{PS} as a function of the concentration x_P determined in the present work and for other II–VI DMS bulk materials. The black line represents the predicted ratio in a model with a dominant AF interaction between first neighbors and based on a random distribution of the magnetic ions; the gray line is the same, but horizontally translated to left (highlighted by the arrow) in order to match the experimental data. (I) From ref. 70, (II) from ref. 89, (III) from ref. 69, (IV) from ref. 73, (V) from ref. 90, (VI) from ref. 72, and (VII) from ref. 91.

For all samples, and below 100 K, the magnetic susceptibility departs from the CW law in the form of a downturn in the graph of the inverse of the paramagnetic susceptibility *versus* temperature (inset of Fig. 7(a)). This feature is much more pronounced for large Co-dopant concentration (x_N) and is due mainly to the AF coupling between two Co^{2+} ions (pairs) and other Co clusters with total spin (S_T) in the ground state equal to zero.[94] The effect of AF clustering is also easily detectable in the magnetization curves measured at T = 4 K displayed in Fig. 7(c). Here, M is normalized to its saturation value M_{PS} (M_{PS} is the theoretical saturation magnetization value considering

no relevant exchange interaction between the Co^{2+} ions, paramagnetic case). M is due mainly to isolated Co^{2+} ions (singles) and AF clusters with $S_T \neq 0$. At higher fields we observe a decrease of the M/M_{PS} values with increasing Co concentration. This feature indicates that the population of singles decreases with increasing Co concentration, as expected by an AF clustering. The magnetization curves of the samples can be well fitted by a modified Brillouin function (MBF).[95] This fit gives the value of the technical saturation magnetization (M_{TS}). Considering a cluster theoretical model with one AF exchange interaction between first Co neighbors, and assuming a random distribution of the magnetic ions over the cation sites, the ratio M_{TS}/M_{PS} can be calculated by

$$M_{TS}/M_{PS} = P_S + P_{OT}/3 + P_{CT}/15 + P_{PQ}/2 + P_{FQ}/5 + P_O/5, \quad (1)$$

where P_i is the probability that a magnetic ion belongs to each of these i type of cluster: S = single, OT = open triplet, CT = closed triplet, PQ = propeller quartet, FQ = funnel quartet, other = cluster larger than quartet. The probabilities P_i as a function of concentration can be determined using the cluster tables given in ref. 96. Fig. 7(d) shows the ratio M_{TS}/M_{PS} as a function of x_P determined for the studied samples and for others based on II–VI DMSs with a wurtzite structure. The line represents the calculated ratio using eqn (1). Previous works on bulk II–VI DMSs agree quite well with the theoretical model. However, for our nanostructured $Zn_{1-x}Co_xO$ samples, the data show a large deviation for lower values of the theoretical curve. By a simple translation of the theoretical curve to lower values in x_P, we observe that the obtained experimental data follow the expected behavior predicted by the theoretical model, but considering higher values of dopant concentration, that we call now local concentration (x_L). The obtained values are: x_L = 0.027, 0.033, 0.053, 0.073 and 0.102 for the samples with x_N = 0.005, 0.01, 0.03, 0.05 and 0.07, respectively. The result $x_L > x_N$ for all samples indicates a clumped distribution of the Co ions, complementing and confirming the previous structural results related to the inhomogeneity distribution of the Co ions over the volume of the nanoparticle, mainly concentrating at its surface. Therefore, the studied nanoparticles can be described as composed of a pure ZnO core covered with a $Zn_{1-x}Co_xO$ layer with Co concentration x_L. Assuming that the Co distribution in the $Zn_{1-x}Co_xO$ layer is random, the diameter of the pure ZnO (d_{ZnO}) core can be determined using $d_{ZnO} = (1 - x_P/x_L)^{1/3} \times d$, where d is the total diameter (Table 3). So, the thickness of the $Zn_{1-x}Co_xO$ layer (e) can then be deduced. We obtained e = 1 nm, 1.1 nm, 2.2 nm, 2.5 nm and 2.8 nm for x_N = 0.005, 0.01, 0.03, 0.05 and 0.07, respectively.

4.6. Growth and doping of the w-ZnO nanoparticle

As presented before, the doping process at the nanoscale has been a matter of debate since the last decade.[26] In this context, two different main models have been discussed, one relates the process to thermodynamic issues, the self-purification effect;[97] the other one states that the doping process is kinetically controlled.[98] In the self-purification model the defect formation energy, the energetic cost for dopant incorporation into the host lattice, increases as the size of the nanoparticle decreases. In the process of nucleation and growth of the nanoparticle the picture corresponds to the formation of a dopant-free core and a subsequent increase of the dopant incorporation as the nanoparticle grows, until the bulk condition is reached. In the other model, the mechanism that controls the doping is the initial adsorption of dopants on the surface of the nanocrystal during its growth determined by the surface morphology, nanocrystal shape and the surfactants in the growth solution. Besides, most recently, Chen *et al.*[99] gave some important contribution to the understanding of the doping process of nanostructured semiconductors. Based on experimental results they proposed that the doping process would be divided into, at least, four different and independent mechanisms: surface adsorption, lattice incorporation, lattice diffusion and lattice ejection.

Here, to address the question, we calculated *via* DFT the formation energy (E_f) for Co incorporation into the w-ZnO nanoparticle, in comparison with the formation energy in the ZnO bulk; we followed the procedure described in ref. 97. We found that the formation energies for the incorporation of Co in the volume (inner region) and in the surface of the nanoparticle are, respectively, 2.99 and 3.52 eV lower than that in the ZnO bulk, suggesting that Co incorporation is easier in the nanoparticle than in the bulk system. These results also indicate that, contrary to what is pointed in ref. 97, the decrease in size favors the doping. Schoenhalz *et al.*[36] have obtained similar results also for Co-doped ZnO nanoparticles; considering non-passivated surfaces they found that the defect formation energy also decreases as the size of the nanoparticle decreases; besides, considering passivated surfaces, they did not obtain any significant changes in the defect formation energy with the size of the nanoparticle. Considering other systems, Li *et al.*[100] have also shown that, for ZnSe doping with isovalent elements (Mn and Mg), the changes in the formation energies as a function of the size of the nanoparticle is relatively small. From our theoretical results and the above comments, we conclude that the self-purification model is not an intrinsic and universal property of defects in nanostructured semiconductors, and that the Co incorporation into the nanostructured ZnO, specifically, would be easier, or at least the same, as compared to bulk ZnO. Once the Co solubility in bulk ZnO samples is relatively high,[101] we would expect a similar behavior at the nanoscale. This assumption is confirmed by the observed degree of doping in our nanostructured samples, around 100%, as $x_N \cong x_E$ (Table 3). Considering the process of dopant surface adsorption and its subsequent incorporation into the lattice of the host matrix separately,[99] these data ($x_N \cong x_E$) give us also some insights into the Co adsorption reaction at the surfaces of the ZnO nanoparticle. In the kinetically controlled model,[98] differences in the dopant binding energy related to different surfaces of the nanoparticles lead to non-homogeneous doping over the nanoparticle volume and, also, to a degree of doping lower than the concentration of the doping element in the growth solution, corresponding to the fraction of the reactive surface with respect to the total surface area of the nanoparticle (taking into account the non/less reactive surfaces). As we are dealing

here with round shaped (multifaceted) nanoparticles (Fig. 2(a)), we can state that the Co binding energy is relatively high and independent of the specific ZnO surface. However, further theoretical studies are necessary in order to corroborate this statement.

Another important result of our calculation is that the E_f is lower at the surface than in the volume of the nanoparticle. These results drive us to investigate about the diffusion barrier energy (E_d) related to Co in the w-ZnO structure. For the nanoparticle simulated here, the diffusion barrier was computed considering three Zn substitutional sites for the Co impurity: in the volume, in the sub-surface and in the surface. We found that the configuration with Co replacing a Zn atom in the volume of the nanoparticle has total energy $\sim$0.53 eV higher than that with Co at a Zn site in the surface, and $\sim$0.06 eV lower than that with Co at a sub-surface site. From these results we estimate that the diffusion barrier for the Co dopant to migrate from the volume to the surface of the nanoparticle (outer direction) is only about 0.06 eV, and in the opposite direction (inner direction), from the surface to the volume, it is 0.59 eV, one order of magnitude higher than that in the outer direction. We can estimate the temperature for Co diffusion by using the transition state theory.[102] Here an atom jumps into a neighboring site across an energy barrier E_d with a frequency (Γ) given by $\Gamma = \Gamma_0 \times \exp(-E_d/k_BT)$, where k_B is the Boltzmann constant and T is the temperature. As suggested by Janotti *et al.*,[103] the temperature at which a defect becomes mobile can be obtained by taking $\Gamma = 1\ s^{-1}$, by the usual definition of that temperature, and $\Gamma_0 = 10^{13}\ s^{-1}$, a typical phonon frequency. With these values and the calculated E_d, we obtain an activation temperature of $\sim$23 K for diffusion from the volume to the surface and $\sim$224 K in the opposite direction. With these data we can state that at the temperature of synthesis, during the nanoparticle growth and the concomitant Co incorporation, the Co ions will easily diffuse along the nanoparticle. However, upon lowering the temperature, the Co ions will be trapped at its surface, as the diffusion barrier to come back to the inner region of the nanoparticle is higher ($\sim$0.59 eV) than that in the outer direction, leading, thus, to the experimentally observed Co enriched nanoparticle passivated surface. Fig. 8 presents a static picture of the ZnO nanoparticle growth and Co incorporation dynamics based on the above assumptions.

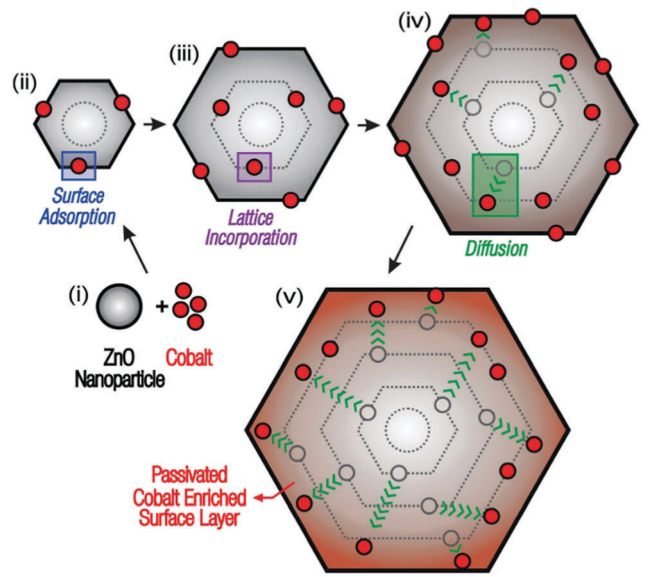

Fig. 8 Cross-sectional view (static picture) of the nucleation and growth of a nanoparticle. (i) For small nanocrystals many semiconductors form non-crystalline cage-like clusters, typically with highly stable surfaces that suppress dopant adsorption.[98] (ii) As the nanoparticle grows, under equilibrium, a faceted nanoparticle evolves and Co ions start adsorbing onto its surface. (iii) In the subsequent growth of the nanoparticle the adsorbed Co ion is incorporated into the ZnO lattice. (iv) Due to the relatively lower value of the E_d the Co ions start to diffuse along the volume of the nanoparticle. (v) Once in the region close to the surface, the Co ions end up trapped as the diffusion barrier back to the inner region of the nanoparticle is higher than that in the outer direction, leading to a passivated Co-enriched surface layer.

5. Conclusions

In summary, we have presented complete structural and magnetic characterization of Co-doped ZnO nanoparticles synthesized *via* a microwave-assisted hydrothermal route. All the results obtained in the structural characterization by the conjugation of different techniques confirm that the Co ions in the nanoparticles substitute the Zn ions in the w-ZnO lattice with oxidation state +2. There was no indication of metallic Co or other secondary foreign phases. Electron microscopy results and state-of-the-art elemental distribution analysis performed *via* EELS reveal that the Co ions are mainly located near/at the surface of the w-ZnO nanoparticles and the Co-rich ZnO surface is passivated. The magnetic data present a combination of a diamagnetic ZnO matrix component associated with a ferromagnetic and a paramagnetic phase. The ferromagnetic phase is observed for the undoped ZnO sample; for the Co-doped ZnO samples, the ferromagnetic phase decreases as the Co content increases. In light of the DFT results, we conclude that the observed RTFM is mainly associated with a surface magnetism and that a Co ferromagnetic order would only be possible at very low Co concentration. These results shed light on the understanding of the nature of the often observed RTFM in the Co-doped w-ZnO system.

The Co concentration in the studied samples measured by EDS (x_E) and the one obtained through the magnetic susceptibility (x_P) are in very good agreement with the nominal concentration (x_N). However, an in-depth analysis of the paramagnetic phase shows that the Co ions are incorporated near/at the surface of the nanoparticles, corroborating the EELS results. Based on the experimental results and DFT calculations of the formation energy and the Co diffusion barrier energy through the nanoparticle, we concluded that the self-purification model is not an intrinsic and universal property of defects in nanostructures, and sketched a kinetic-thermodynamic model of the growth and Co-doping process of the ZnO nanoparticles. The results presented in this report give a valuable contribution to

the knowledge of the synthesis of doped nanoparticles for potential applications in different technological areas. This work also illustrates how the study of the magnetic properties, besides its natural importance, can give us very useful information about the doping elemental distribution at the nanoscale.

Conflicts of interest

There are no conflicts to declare.

Acknowledgements

Support from agencies FAPEMIG (PPM-00533-16; APQ-00273-14; RED-00010-14), CNPq (470069/2013-9; 448723/2014-0; 308162/2015-3, 306065/2015-0), FAPESP (2013/07909-4; 2015/16191-5) and CAPES (PNPD-2011) is gratefully acknowledged. We also thank CNPq (WAAM, MIBB and ACD) and CAPES (NCM, AOZ) for research fellowships. We thank Red Española de Supercomputación (Proyect ID: QCM-2014-1-0036) and CENAPAD/SP (Brazil) for computing facilities. The authors also acknowledge Prof. Dr F. Iikawa and Prof. Dra. M. J. S. Brasil of the Universidade de Campinas (UNICAMP) for Raman measurements and Dr Jefferson Bettini of the Brazilian Nanotechnology National Laboratory (LNNano) for the EELS analysis.

References

1 A. Teke, U. Ozgur, S. Dogan, X. Gu, H. Morkoc, B. Nemeth, J. Nause and H. O. Everitt, *Phys. Rev. B: Condens. Matter Mater. Phys.*, 2004, **70**, 195207.
2 G. C. Deng, A. L. Ding, W. X. Cheng, X. S. Zheng and P. S. Qiu, *Solid State Commun.*, 2005, **134**, 283–286.
3 J. H. Lee, K. H. Ko and B. O. Park, *J. Cryst. Growth*, 2003, **247**, 119–125.
4 R. Ullah and J. Dutta, *J. Hazard. Mater.*, 2008, **156**, 194–200.
5 Y. T. Kim, J. Park, S. Kim, D. W. Park and J. Choi, *Electrochim. Acta*, 2012, **78**, 417–421.
6 M. Ohtaki, *J. Ceram. Soc. Jpn.*, 2011, **119**, 770–775.
7 B. Kumar and S. W. Kim, *Nano Energy*, 2012, **1**, 342–355.
8 D. T. Phan and G. S. Chung, *Sens. Actuators, B*, 2012, **161**, 341–348.
9 H. M. Xiong, *Adv. Mater.*, 2013, **25**, 5329–5335.
10 S. B. Rana and R. P. P. Singh, *J. Mater. Sci.: Mater. Electron.*, 2016, **27**, 9346–9355.
11 D. Y. Inamdar, A. K. Pathak, I. Dubenko, N. Ali and S. Mahamuni, *J. Phys. Chem. C*, 2011, **115**, 23671–23676.
12 S. Kumar, S. Chatterjee, K. K. Chattopadhyay and A. K. Ghosh, *J. Phys. Chem. C*, 2012, **116**, 16700–16708.
13 S. B. Rana, *J. Mater. Sci.: Mater. Electron.*, 2017, **28**, 13787–13796.
14 I. Zutic, J. Fabian and S. Das Sarma, *Rev. Mod. Phys.*, 2004, **76**, 323–410.
15 T. Dietl, H. Ohno, F. Matsukura, J. Cibert and D. Ferrand, *Science*, 2000, **287**, 1019–1022.
16 H. B. de Carvalho, M. P. F. de Godoy, R. W. D. Paes, M. Mir, A. Ortiz de Zevallos, F. Iikawa, M. J. S. P. Brasil, V. A. Chitta, W. B. Ferraz, M. A. Boselli and A. C. S. Sabioni, *J. Appl. Phys.*, 2010, **108**, 033914.
17 S. Kolesnik, B. Dabrowski and J. Mais, *J. Appl. Phys.*, 2004, **95**, 2582–2586.
18 M. P. F. de Godoy, A. Mesquita, W. Avansi, P. P. Neves, V. A. Chitta, W. B. Ferraz, M. A. Boselli, A. C. S. Sabioni and H. B. de Carvalho, *J. Alloys Compd.*, 2013, **555**, 315–319.
19 V. M. de Almeida, A. Mesquita, A. O. de Zevallos, N. C. Mamani, P. P. Neves, X. Gratens, V. A. Chitta, W. B. Ferraz, A. C. Doriguetto, A. C. S. Sabioni and H. B. de Carvalho, *J. Alloys Compd.*, 2016, **655**, 406–414.
20 N. C. Mamani, R. T. da Silva, A. O. de Zevallos, A. A. C. Cotta, W. A. D. Macedo, M. S. Li, M. I. B. Bernardi, A. C. Doriguetto and H. B. de Carvalho, *J. Alloys Compd.*, 2017, **695**, 2682–2688.
21 G. Rahman, V. M. Garcia-Suarez and S. C. Hong, *Phys. Rev. B: Condens. Matter Mater. Phys.*, 2008, **78**, 184404.
22 G. Rahman, N. U. Din, V. M. Garcia-Suarez and E. Kan, *Phys. Rev. B: Condens. Matter Mater. Phys.*, 2013, **87**, 205205.
23 R. P. P. Singh, I. S. Hudiara, S. Panday and S. B. Rana, *J. Supercond. Novel Magn.*, 2016, **29**, 819–827.
24 J. D. Bryan and D. R. Gamelin, *Prog. Inorg. Chem.*, 2005, **54**, 47–126.
25 A. L. Efros, E. I. Rashba and M. Rosen, *Phys. Rev. Lett.*, 2001, **87**, 206601.
26 D. J. Norris, A. L. Efros and S. C. Erwin, *Science*, 2008, **319**, 1776–1779.
27 J. F. Suyver, S. F. Wuister, J. J. Kelly and A. Meijerink, *Phys. Chem. Chem. Phys.*, 2000, **2**, 5445–5448.
28 M. I. B. Bernardi, A. Mesquita, F. Beron, K. R. Pirota, A. O. de Zevallos, A. C. Doriguetto and H. B. de Carvalho, *Phys. Chem. Chem. Phys.*, 2015, **17**, 3072–3080.
29 A. C. Larson and R. B. V. Dreele, *Los Alamos National Laboratory Report LAUR*, 1994, pp. 86–748.
30 B. H. Toby, *J. Appl. Crystallogr.*, 2001, **34**, 210–213.
31 A. Michalowicz, J. Moscovici, D. Muller-Bouvet and K. Provost, *J. Phys.: Conf. Ser.*, 2009, **190**, 012034.
32 A. L. Ankudinov, B. Ravel, J. J. Rehr and S. D. Conradson, *Phys. Rev. B: Condens. Matter Mater. Phys.*, 1998, **58**, 7565–7576.
33 P. Hohenberg and W. Kohn, *Phys. Rev. B: Condens. Matter Mater. Phys.*, 1964, **136**, B864–B871.
34 W. Kohn and L. J. Sham, *Phys. Rev.*, 1965, **140**, A1133–A1138.
35 J. P. Perdew and A. Zunger, *Phys. Rev. B: Condens. Matter Mater. Phys.*, 1981, **23**, 5048–5079.
36 A. L. Schoenhalz and G. M. Dalpian, *Phys. Chem. Chem. Phys.*, 2013, **15**, 15863–15868.
37 A. L. Schoenhalz, J. T. Arantes, A. Fazzio and G. M. Dalpian, *Appl. Phys. Lett.*, 2009, **94**, 162503.
38 J. M. Soler, E. Artacho, J. D. Gale, A. Garcia, J. Junquera, P. Ordejon and D. Sanchez-Portal, *J. Phys.: Condens. Matter*, 2002, **14**, 2745–2779.
39 N. Troullier and J. L. Martins, *Phys. Rev. B: Condens. Matter Mater. Phys.*, 1991, **43**, 1993–2006.

40 S. C. Abrahams and J. L. Bernstei, *Acta Crystallogr., Sect. B: Struct. Sci.*, 1969, **25**, 1233–1236.
41 R. Shannon, *Acta Crystallogr., Sect. A: Cryst. Phys., Diffr., Theor. Gen. Crystallogr.*, 1976, **32**, 751–767.
42 D. A. Schwartz, N. S. Norberg, Q. P. Nguyen, J. M. Parker and D. R. Gamelin, *J. Am. Chem. Soc.*, 2003, **125**, 13205–13218.
43 X. Gratens, E. ter Haar, V. Bindilatti, N. Oliveira, Y. Shapira, M. Liu, Z. Golacki, S. Charar and A. Errebbahi, *J. Phys.: Condens. Matter*, 2000, **12**, 3711–3718.
44 M. Pal, U. Pal, J. Jimenez and F. Perez-Rodriguez, *Nanoscale Res. Lett.*, 2012, **7**, 1–12.
45 M. Scepanovic, S. Askrabic, V. Berec, A. Golubovic, Z. Dohcevic-Mitrovic, A. Kremenovic and Z. V. Popovic, *Acta Phys. Pol., A*, 2009, **115**, 771–774.
46 X. F. Wang, F. Q. Song, Q. Chen, T. Y. Wang, J. L. Wang, P. Liu, M. R. Shen, J. G. Wan, G. H. Wang and J. B. Xu, *J. Am. Chem. Soc.*, 2010, **132**, 6492–6497.
47 T. Sugimoto, *Monodispersed Particles*, Elsevier, Amsterdam, 2001.
48 L. Guo, S. H. Yang, C. L. Yang, P. Yu, J. N. Wang, W. K. Ge and G. K. L. Wong, *Chem. Mater.*, 2000, **12**, 2268–2274.
49 R. Viswanatha and D. D. Sarma, *Chem. – Eur. J.*, 2006, **12**, 180–186.
50 N. S. Pesika, Z. S. Hu, K. J. Stebe and P. C. Searson, *J. Phys. Chem. B*, 2002, **106**, 6985–6990.
51 R. L. He, R. K. Hocking and T. Tsuzuki, *Mater. Chem. Phys.*, 2012, **132**, 1035–1040.
52 J. Kaur and S. Singhal, *Ceram. Int.*, 2014, **40**, 7417–7424.
53 K. C. Barick, S. Singh, M. Aslam and D. Bahadur, *Microporous Mesoporous Mater.*, 2010, **134**, 195–202.
54 R. Cusco, E. Alarcon-Llado, J. Ibanez, L. Artus, J. Jimenez, B. Wang and M. J. Callahan, *Phys. Rev. B: Condens. Matter Mater. Phys.*, 2007, **75**, 165202.
55 F. Friedrich and N. H. Nickel, *Appl. Phys. Lett.*, 2007, **91**, 111903.
56 F. Reuss, C. Kirchner, T. Gruber, R. Kling, S. Maschek, W. Limmer, A. Waag and P. Ziemann, *J. Appl. Phys.*, 2004, **95**, 3385–3390.
57 Z. Q. Chen, A. Kawasuso, Y. Xu, H. Naramoto, X. L. Yuan, T. Sekiguchi, R. Suzuki and T. Ohdaira, *J. Appl. Phys.*, 2005, **97**, 013528.
58 M. Schumm, M. Koerdel, S. Muller, H. Zutz, C. Ronning, J. Stehr, D. M. Hofmann and J. Geurts, *New J. Phys.*, 2008, **10**, 043004.
59 G. J. Huang, J. B. Wang, X. L. Zhong, G. C. Zhou and H. L. Yan, *J. Mater. Sci.*, 2007, **42**, 6464–6468.
60 L. H. Hoang, N. T. M. Hien, N. H. Hai, P. V. Hai, N. T. Khoi and I. S. Yang, *J. Raman Spectrosc.*, 2009, **40**, 1535–1538.
61 J. W. Tringe, H. W. Levie, S. K. McCall, N. E. Teslich, M. A. Wall, C. A. Orme and M. J. Matthews, *Appl. Phys. A: Mater. Sci. Process.*, 2012, **109**, 15–23.
62 J. Zuo, C. Y. Xu, L. H. Zhang, B. K. Xu and R. Wu, *J. Raman Spectrosc.*, 2001, **32**, 979–981.
63 M. Scepanovic, M. Grujic-Brojcin, K. Vojisavljevic, S. Bernik and T. Sreckovic, *J. Raman Spectrosc.*, 2010, **41**, 914–921.
64 S. Ghose, T. Rakshit, R. Ranganathan and D. Jana, *RSC Adv.*, 2015, **5**, 99766–99774.
65 R. H. Callender, S. S. Sussman, M. Selders and R. K. Chang, *Phys. Rev. B: Solid State*, 1973, **7**, 3788–3798.
66 P. J. Colwell and M. V. Klein, *Solid State Commun.*, 1970, **8**, 2095–2100.
67 J. Pellicer-Porres, A. Segura, J. F. Sanchez-Royo, J. A. Sans, J. P. Itie, A. M. Flank, P. Lagarde and A. Polian, *Superlattices Microstruct.*, 2007, **42**, 251–254.
68 L. R. Valério, N. C. Maman, A. O. de Zevallos, A. Mesquita, M. I. B. Bernardi, A. C. Doriguetto and H. B. de Carvalho, *RSC Adv.*, 2017, **7**, 20611–20619.
69 X. Gratens, V. Bindilatti, N. F. Oliveira, Y. Shapira, S. Foner, Z. Golacki and T. E. Haas, *Phys. Rev. B: Condens. Matter Mater. Phys.*, 2004, **69**, 125209.
70 M. Bouloudenine, N. Viart, S. Colis, J. Kortus and A. Dinia, *Appl. Phys. Lett.*, 2005, **87**, 052501.
71 T. E. de Souza, A. Mesquita, A. O. de Zevallos, F. Beron, K. R. Pirota, P. P. Neves, A. C. Doriguetto and H. B. de Carvalho, *J. Phys. Chem. C*, 2013, **117**, 13252–13260.
72 C. J. Chen, M. Qu, W. Hu, X. Zhang, F. Lin, H. B. Hu, K. J. Ma and W. Giriat, *J. Appl. Phys.*, 1991, **69**, 6114–6116.
73 D. Heiman, Y. Shapira, S. Foner, B. Khazai, R. Kershaw, K. Dwight and A. Wold, *Phys. Rev. B: Condens. Matter Mater. Phys.*, 1984, **29**, 5634–5640.
74 A. Sundaresan, R. Bhargavi, N. Rangarajan, U. Siddesh and C. N. R. Rao, *Phys. Rev. B: Condens. Matter Mater. Phys.*, 2006, **74**, 161306.
75 S. Banerjee, M. Mandal, N. Gayathri and M. Sardar, *Appl. Phys. Lett.*, 2007, **91**, 182501.
76 J. M. D. Coey, *Solid State Sci.*, 2005, **7**, 660–667.
77 G. Z. Xing, D. D. Wang, J. B. Yi, L. L. Yang, M. Gao, M. He, J. H. Yang, J. Ding, T. C. Sum and T. Wu, *Appl. Phys. Lett.*, 2010, **96**, 112511.
78 D. Q. Gao, Z. H. Zhang, J. L. Fu, Y. Xu, J. Qi and D. S. Xue, *J. Appl. Phys.*, 2009, **105**, 113928.
79 X. Y. Xu, C. X. Xu, J. Dai, J. G. Hu, F. J. Li and S. Zhang, *J. Phys. Chem. C*, 2012, **116**, 8813–8818.
80 N. H. Hong, J. Sakai and V. Brize, *J. Phys.: Condens. Matter*, 2007, **19**, 036219.
81 J. B. Yi, C. C. Lim, G. Z. Xing, H. M. Fan, L. H. Van, S. L. Huang, K. S. Yang, X. L. Huang, X. B. Qin, B. Y. Wang, T. Wu, L. Wang, H. T. Zhang, X. Y. Gao, T. Liu, A. T. S. Wee, Y. P. Feng and J. Ding, *Phys. Rev. Lett.*, 2010, **104**, 137201.
82 M. Khalid, M. Ziese, A. Setzer, P. Esquinazi, M. Lorenz, H. Hochmuth, M. Grundmann, D. Spemann, T. Butz, G. Brauer, W. Anwand, G. Fischer, W. A. Adeagbo, W. Hergert and A. Ernst, *Phys. Rev. B: Condens. Matter Mater. Phys.*, 2009, **80**, 035331.
83 X. B. Chen, G. S. Li, Y. G. Su, X. Q. Qiu, L. P. Li and Z. G. Zou, *Nanotechnology*, 2009, **20**, 115606.
84 A. Y. Yermakov, G. S. Zakharova, M. A. Uimin, M. V. Kuznetsov, L. S. Molochnikov, S. F. Konev, A. S. Konev, A. S. Minin, V. V. Mesilov, V. R. Galakhov, A. S. Volegov, A. V. Korolyov, A. F. Gubkin, A. M. Murzakayev, A. D. Svyazhin and K. V. Melanin, *J. Phys. Chem. C*, 2016, **120**, 28857–28866.

85 J. M. D. Coey, M. Venkatesan and P. Stamenov, *J. Phys.: Condens. Matter*, 2016, **28**, 485001.
86 G. S. Chang, J. Forrest, E. Z. Kurmaev, A. N. Morozovska, M. D. Glinchuk, J. A. McLeod, A. Moewes, T. P. Surkova and N. H. Hong, *Phys. Rev. B: Condens. Matter Mater. Phys.*, 2012, **85**, 165319.
87 P. Sati, R. Hayn, R. Kuzian, S. Regnier, S. Schafer, A. Stepanov, C. Morhain, C. Deparis, M. Laugt, M. Goiran and Z. Golacki, *Phys. Rev. Lett.*, 2006, **96**, 017203.
88 N. Jedrecy, H. J. von Bardeleben, Y. Zheng and J. L. Cantin, *Phys. Rev. B: Condens. Matter Mater. Phys.*, 2004, **69**, 041308.
89 S. J. Han, B. Y. Lee, J. S. Ku, Y. B. Kim and Y. H. Jeong, *J. Magn. Magn. Mater.*, 2004, **272**, 2008–2009.
90 D. Heiman, Y. Shapira and S. Foner, *Solid State Commun.*, 1983, **45**, 899–902.
91 M. Nawrocki, R. Planel, F. Mollot and M. J. Kozielski, *Phys. Status Solidi B*, 1984, **123**, 99–103.
92 S. Yin, M. X. Xu, L. Yang, J. F. Liu, H. Rosner, H. Hahn, H. Gleiter, D. Schild, S. Doyle, T. Liu, T. D. Hu, E. Takayama-Muromachi and J. Z. Jiang, *Phys. Rev. B: Condens. Matter Mater. Phys.*, 2006, **73**, 224408.
93 L. B. Duan, W. G. Chu, J. Yu, Y. C. Wang, L. N. Zhang, G. Y. Liu, J. K. Liang and G. H. Rao, *J. Magn. Magn. Mater.*, 2008, **320**, 1573–1581.
94 Y. Shapira and V. Bindilatti, *J. Appl. Phys.*, 2002, **92**, 4155–4185.
95 J. A. Gaj, R. Planel and G. Fishman, *Solid State Commun.*, 1979, **29**, 435–438.
96 The cluster tables are given in the EPAPS document at the homepage http://ftp.aip.org/epaps/app_phys_rev/E-JAPIAU-92-110220/.
97 G. M. Dalpian and J. R. Chelikowsky, *Phys. Rev. Lett.*, 2006, **96**, 226802.
98 S. C. Erwin, L. J. Zu, M. I. Haftel, A. L. Efros, T. A. Kennedy and D. J. Norris, *Nature*, 2005, **436**, 91–94.
99 D. A. Chen, R. Viswanatha, G. L. Ong, R. G. Xie, M. Balasubramaninan and X. G. Peng, *J. Am. Chem. Soc.*, 2009, **131**, 9333–9339.
100 J. B. Li, S. H. Wei, S. S. Li and J. B. Xia, *Phys. Rev. B: Condens. Matter Mater. Phys.*, 2008, **77**, 113304.
101 A. Mesquita, F. P. Rhodes, R. T. da Silva, P. P. Neves, A. O. de Zevallos, M. R. B. Andreeta, M. M. de Lima Jr., A. Cantarero, I. S. da Silva, M. A. Boselli, X. Gratens, V. A. Chitta, A. C. Doriguetto, W. B. Ferraz, A. C. S. Sabioni and H. B. de Carvalho, *J. Alloys Compd.*, 2015, **637**, 407–417.
102 G. H. Vineyard, *J. Phys. Chem. Solids*, 1957, **3**, 121–127.
103 A. Janotti and C. G. Van de Walle, *Phys. Rev. B: Condens. Matter Mater. Phys.*, 2007, **76**, 165202.